Validation of CFD Simulations of a Stirred Tank Using Particle Image Velocimetry Data

JIAN SHENG, HUI MENG and RODNEY O. FOX+*

Program for Complex Fluid Flows, Kansas State University, Manhattan, KS 66506

Methods for validating CFD simulations based on the Reynolds Average Navier-Stokes equation (RANS) against Particle Image Velocimetry (PIV) measurements are investigated and applied to one of the most common problems in the chemical process industry – the prediction of flow field in a stirred vessel. A total of 1024 sequential instantaneous 2D velocity fields along the central axial plane of a stirred vessel with a P-4 axial impeller are obtained through PIV measurement. From the PIV data, the mean velocity, turbulent kinetic energy, Reynolds stresses and dissipation rate fields are extracted. By introducing several tools to quantify the similarities and differences between two-dimensional fields, CFD predictions of the flow field are validated against PIV data. Furthermore, using PIV and LDV data, the effect of boundary conditions on CFD simulation results is examined. The effect of different Reynolds stress closures on the flow prediction is also studied.

Des méthodes de validation de simulations numériques (CFD) d'écoulements turbulents représentés par l'équation de Navier-Stokes modifié (Reynolds-Average Navier Stokes) comparées à des mesures de vélocimétrie par imagerie de particules (PIV), sont étudiées et appliquées à l'un des problèmes les plus fréquents de l'industrie chimique – la prédiction du champ d'écoulement dans un réservoir agité. Au total, 1024 champs de vitesse 2D instantanés séquentiels le long du plan axial central d'un réservoir agité muni d'une turbine axiale P-4, sont obtenus par des mesures de PIV. De ces mesures sont extraits la vitesse moyenne, l'énergie cinétique turbulente, les contraintes de Reynolds et les taux de dissipation. En introduisant plusieurs outils pour quantifier les similtudes et différences entre des champs bidimensionnels, les prédictions numériques du champ d'écoulement sont validées par comparaison à des données de PIV. En outre, à l'aide de données de PIV et de LDV, l'effet des conditions limites dans les simulations numériques est examiné. L'effet de différentes conditions de fermeture des contraintes de Reynolds sur la prédiction des écoulements est également étudié.

Keywords: computation fluid dynamics, particle image velocimetry, stirred tank, CFD validation.

Computational Fluid Dynamics (CFD) is now widely used to predict flow fields in industrial mixers owing to its short turn-over time and low cost. However, uncertainties in CFD predictions exist for complex flows such as flows with complex geometry, time-dependency, and turbulence. This is not only because we usually cannot prescribe the boundary conditions and initial conditions well enough for the computational solver due to lack of accurate experimental data input, but, in the case of turbulence, also because of inherent deficiencies in turbulence models used in the CFD codes.

Currently practical CFD models for turbulent flows are based on solving Reynolds Averaged Navier Stokes Equations (RANS) with turbulence models (closures). Although steady turbulent flows can be described by the simulated time-averaged flow fields to some extent, mixing processes are mostly unsteady, exhibiting large-scale instabilities as in the case of stirred tanks (Bakker et al. 1996). In particular, organized vortical structures such as trailing vorticies (Calabrese and Stoots 1989, Stoots and Calabrese, 1995) related to periodical blade passage (Wu and Petterson 1989, Kresta and Wood 1993) dominate the flow, rendering it highly anisotropic. Especially prominent is the anisotropy effect in the discharge region of a stirred vessel as found by Yianneskis et al. (1987), Calabrese and Stoots (1989), van't Riet and Smith (1975), van't Riet et al. (1975), and Rao and Brodkey (1972). On the other hand, two-equation turbulence models used in CFD such as the k-ε Model and the k-ε RNG Model are all based on isotropic turbulence. This inaccurate assumption, together with the difficulty in prescribing the boundary conditions for complex geometry, brings large uncertainties in the CFD predictions in complex flows such as impeller stirred vessels. Clearly, to improve CFD prediction accuracy and thus confidence in design scale-up, CFD simulations need to be validated against detailed experimental data.

The stirred vessel is one of the oldest and most commonly encountered industrial devices. It is frequently used in chemical process industry where gas dispersion in liquids, liquid-liquid blending and solid suspensions in liquids are involved. With the application of CFD, the process variables such as mean velocity distribution, time scales, distribution of kinetic energy and dissipation rate can be obtained from CFD simulation on the time-averaged level. Numerical investigations of this complex fluid flow has been conducted by many researchers (Bakker and van den Akker 1994, Bakker et al. 1996, Ranade and Joshi 1990, Kresta and Wood 1991, Xu and McGrath 1996, and Fokema et al. 1994).

The flow characteristics of stirred vessels have been studied through single-point LDV methods in the past (Rao and Brodkey, 1972; Van't Riet and Smith, 1975, Yianneskis et al., 1987; Calabrese and Stoots, 1989, Wu and Petterson 1989, Wu et al., 1989; Kresta and Wood, 1993). Nevertheless, the flow in a stirred tank is highly unsteady, and time-varying large scale motions dominate the flow. Bakker et al. (1996) and Ward (1995) were the first to use Particle Image Velocimetry (PIV) to study the two-dimensional (2D) flow pattern along a center plane in this tank. They found bimodal and trimodal distributions in the ensemble-averaged velocity in certain regions. Instantaneous PIV measurement reveals

---

*Author to whom correspondence should be addressed. Department of Mechanical and Nuclear Engineering, Kansas State University, Rathbone Hall, Manhattan, KS 66506. E-mail address: meng@ksume.me.ksu.edu.

+Department of Chemical Engineering, Durland Hall, Manhattan KS 66506.

the presence of large scale flow pattern instabilities with a time scale much longer than the impeller rotation frequency, which suggests that the flow is highly three-dimensional and chaotic in nature.

Clearly, for the stirred vessel as for all other complex flows, there is a need for detailed full-field experimental data to (1) obtain a clear physical picture of the flow, (2) provide necessary guidance in turbulence modeling, boundary condition input and numerical schemes to solve the CFD codes, and (3) to validate and improve CFD simulations. Two-dimensional PIV provides an important tool for obtaining such data. With abundant space- and time-resolved velocity field data from PIV, new insight has been obtained for complex turbulent flows. It is also possible to analyze PIV- flow field data for comparison with CFD simulations.

It should be recognized that PIV is quite different from LDV in that it provides instantaneous velocity field snapshots in a plane (or in a volume in the case of holographic PIV) as opposed to a single point, albeit at a much lower sampling rate in time (usually limited to 10–30 Hz) than LDV (up to 20 kHz). Hence, PIV provides overall flow fields with spatially resolved eddies but low temporal resolution. As a result, if we use PIV to obtain single-point statistics, the high frequency velocity fluctuations may be lost. However, the gain of instantaneous spatial resolution obtained through PIV outweighs this loss. For example, we no longer need to rely on Taylor's hypothesis to approximate the spatial variations from time-resolved single-point measurements. Spatial derivatives, such as terms in turbulence dissipation rate, can be directly estimated from the space resolved PIV velocity fields. Hence, PIV is a good tool to validate full-field CFD simulations.

In the present work, we analyze PIV data obtained in a baffled cylindrical stirred vessel with a 45° pitched blade turbine (PBT) axial impeller operating in the turbulent regime. For the same flow, we have conducted CFD simulations using the k-ε RNG model and a full second-moment Reynolds Stress Model (RSM). The main objective of this study is to provide preliminary tools for CFD validation using full-field experimental measurement and shake out potential problems. Since practical CFD methods solve time-averaged Navier-Stokes equations, at the present we can only compare experiments and CFD at the statistical level. In this regard, we develop methods to extract statistical information from the PIV data and to quantitatively compare them with simulation results. Obviously, to fully characterize this highly three-dimensional flow, we need 3D full-field data. Without the out-of-plane component in the PIV data, one has to withhold judgment to a large extent about the CFD prediction accuracy. Nonetheless, we believe that this study points to new opportunities.

PIV experimental setup

The PIV experiment was described in detail by Ward (1995) and reported by Bakker et al. (1996). The axial impeller stirred vessel was a plexiglas circular water tank of diameter T = 0.292 m with the fluid height maintained at 0.311 m. Four axial baffles (width = 0.0243 m) were mounted along the wall as shown in the Figure 1. A P-4 impeller of diameter D = 0.102 m with 45° pitch was located at a height C = 0.134 m from the bottom. The ratio between the vessel and the impeller diameter was D/T = 0.35 and the off bottom clearance was C/T = 0.46. The ratio of blade width (W) to the impeller diameter (D) was 0.20. The impeller was driven at 60 rpm, resulting in a Reynolds number of about 9 200 based on impeller diameter and tip velocity. The integral length scale is determined by half of the blade width ($W/2$) (Kresta and Wood 1993, Rao and Brodkey 1972, Wu and Petterson 1989 and Wu et al. 1989). It is $D/10$ cr 0.01 m. The Kolmogorov length scale estimated from Reynolds number based on integral length scale, $\eta = Re_L^{-3/4}$, is 100 μm.

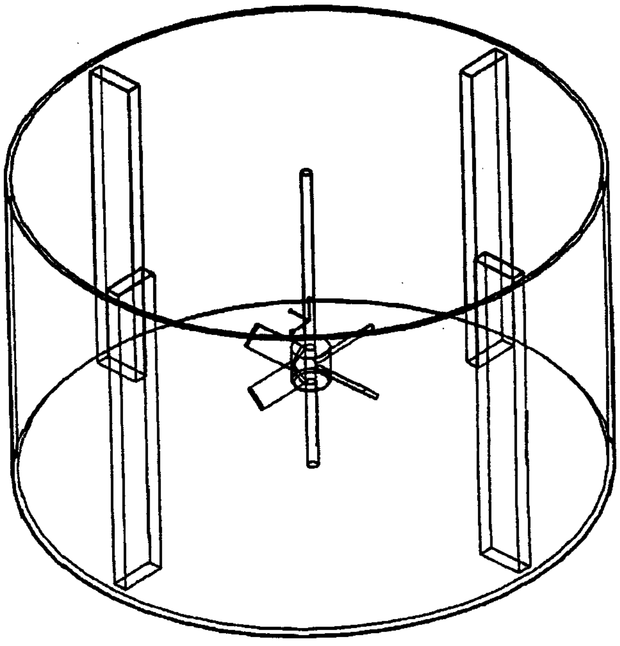

Figure 1 – Sketch of a stirred vessel with a 45° pitched blade turbine (Chemineer P-4 impeller).

The PIV system was a Dantec Flowgrabber™ owned by Chemineer, Inc. As light source an Argon Ion laser was used to produce a 10 mm thick light sheet, which illuminated the tank from the side. To compensate the refractive index variation, the circular tank was kept inside a square tank filled with a compensating liquid. The light sheet position was offset by 10 mm from the center plane to avoid the shaft from blocking the illumination. An 8-bit, black-and-white 512 × 480 CCD camera was used to acquire particle images. The total viewing area is set at 0.292 m × 0.311 m, which yields a spatial resolution of 0.6 mm/pixel. The flow was seeded with 0.1 g of neutrally buoyant 80 μm diameter fluorescent polymer spheres, resulting in a seeding density of 15 to 25 particles in a 16 × 16 pixel sampling window. Two consecutive images are cross-correlated to give the velocity field. A total of 59 × 50 vectors were given for the entire plane at each instant on a changing grid. The average spatial resolution of the vector is roughly 5 mm. A total of 1 024 instantaneous measurements are carried out over a period of 22 min with the sampling rate of 0.77 Hz. More details of the experimental setup can be found in Ward (1995).

PIV data analysis

In this study we start by analyzing the PIV data acquired in the aforementioned experiment by extracting the mean velocity field and turbulence characteristics from the two-dimensional instantaneous planar velocity fields. The purpose of performing time-averaging is to compare with CFD predictions, which are based on time-averaged flow fields.

First, to obtain time-average statistics, one must be concerned with the validity of stationarity and convergence of the statistical measurements. Sequential PIV measurements do not imply that the measurements are time-resolved. In fact, the fastest events in this flow happened at about 4 kHz. In this sense, the measurements should be considered quasi-independent realizations. We validated stationarity of the PIV measurements. Our study shows that after 600 samples, the mean velocity field converged. After about 800 samples, higher order statistics such as Reynolds stresses, kinetic energy, etc. converged. Therefore, although 1024 realizations may seem relatively small, they are sufficient for statistical stationarity and convergence.

In the current and most other commercial PIV systems, the method of extracting the velocity information from PIV images is based on correlation between two particle fields recorded at two exposures. The calculation is carried out over a finite area, referred to as interrogation cell (IC). Each IC provides one velocity vector resulting from spatial averaging of the displacements of particles contained in the IC. From a signal processing point of view, the correlation technique works as a low pass filter and thus has a smoothing effect on the extracted velocity field. Evidently, scales smaller than IC cannot be resolved. Moreover, the smoothing effect of the low pass filter reduces large velocity fluctuations between adjacent IC's.

Since the PIV-resolved velocity is not the same as the real velocity at a single point, care needs to be taken when we analyze PIV data by performing time-averaging. The real velocity vector, u_i, of the flow can be written in terms of resolved (filtered) PIV measurement, $\overline{U}_i$, and a correction term:

$$u_i = \overline{U}_i + O\left(\frac{\Delta^2}{L^2}\right) \quad \dots\dots\dots\dots\dots\dots (1)$$

where L is the integral length scale and Δ is filter width (equivalent to IC size in PIV measurement). Therefore, the real velocity can be approximated along the time axis by PIV measurements when the correction term is far less than 1, that is, when the IC size is small compared to the integral scale. Under this condition, the following approximations can be made:

$$\langle u_i \rangle \approx \langle \overline{U}_i \rangle, \quad \dots\dots\dots\dots\dots\dots (2)$$

$$u_i' \approx \overline{U}_i - \langle \overline{U}_i \rangle, \quad \dots\dots\dots\dots\dots\dots (3)$$

$$\langle u_i' u_j' \rangle \approx \left\langle \left(\overline{U}_i - \langle \overline{U}_i \rangle\right)\left(\overline{U}_j - \langle \overline{U}_j \rangle\right) \right\rangle, \quad \dots\dots\dots (4)$$

where "$\langle\ \rangle$" denotes time-averaging. In our case, the scaling factor Δ/L is equal to 1/32, therefore, the condition of approximation does hold. The statistical quantities, such as mean velocity, turbulent kinetic energy, and turbulence dissipation rate, are obtained directly from PIV data (i.e. $u = u_1$, $v = u_2$, while $w = u_3$ is not available) at the resolved scale, Δ = 5 mm.

The 2D mean velocity field along the center axial plane, with radial component $U(x, y)$ and axial component $V(x, y)$, was obtained by averaging 1 024 sequential instantaneous PIV measurements $u(x,y,t_n)$, $v(x,y,t_n)$, n = 1,2, ..., 1 024. The out-of-plane or circumferential velocity component w was unavailable from the measurement due to the limitations of 2D PIV. Consequently, quantities associated with w or variation of u, v along the z axis were not available or had to be approximated.

Time averaging 1 024 sequential PIV measurement, the mean velocity field in the stirred vessel along the plane of illumination was obtained. An asymmetry in the data about the axis was apparent for velocity vectors near the shaft region (x/T = 0.5). It appeared as though an unexpected radial velocity component was superimposed onto the axial flow along the center plane of the vessel. This effect can be attributed to the offset of the PIV interrogation plane from the center plane of the stirred vessel, introduced during the experiment so that the light sheet was not blocked by the shaft. To remove this artifact, a mirroring procedure was applied to the averaged velocity field along the center plane. The mirroring procedure is defined by the following equations:

$$\begin{aligned} U(x,y) &= \left[U(x,y) - U(T-x,y)\right]/2 \\ V(x,y) &= \left[V(x,y) + V(T-x,y)\right]/2 \end{aligned}, \quad \dots\dots\dots (5)$$

where $U(x)$ and $V(x)$ are the radial and axial mean velocity components at point x; and T is the vessel diameter. It was also assumed that the flow was statistically symmetric about the axis. The corrected mean velocity field is given in Figure 2.

Turbulence kinetic energy is defined by

$$k = \tfrac{1}{2}\left(\left\langle u_1'^2 \right\rangle + \left\langle u_2'^2 \right\rangle + \left\langle u_3'^2 \right\rangle\right). \quad \dots\dots\dots (6)$$

Accurate estimation of kinetic energy requires information about all three components of velocity. Since the axial impeller stirred vessel flow is highly 3D, we cannot completely determine the turbulent kinetic energy with the information from only 2 components of velocity (i = 1,2) measured by PIV. An approximation procedure is thus required to account for the contribution of u_3'. We evoke the local isotropy condition under which the normal stresses of fluctuation velocity are equal, $u_1'\,u_1' \approx u_2'\,u_2' \approx u_3'\,u_3'$. Thus $u_3'\,u_3' \approx \frac{1}{2}(u_1'\,u_1' + u_2'\,u_2')$, and the turbulent kinetic energy can be rewritten as:

$$k = \tfrac{3}{4}\left(\left\langle u_1'^2 \right\rangle + \left\langle u_2'^2 \right\rangle\right). \quad \dots\dots\dots\dots\dots (7)$$

Reynolds stresses, $\langle u_i' u_j' \rangle$ were estimated directly from the 1024 instantaneous velocity measurements. With only i,j = 1,2 available in the PIV measurement, it was possible to obtain only four out of the nine terms in the Reynolds stress tensors. Furthermore, due to the low sampling rate of the PIV measurement (0.77 Hz) and the offset of illumination light sheet, we expect the measured Reynolds stresses to exhibit some asymmetry.

For turbulence dissipation rate ε, which is one of the most important quantities in mixing, we can directly calculate it based on its definition $\varepsilon = 2\nu\langle s_{ij}'\, s_{ij}' \rangle$ if the PIV measurement resolves the velocity field down to the Kolmogorov scale. However, this is usually not the case: to obtain a large viewing area the PIV spatial resolution often falls in the inertial range. To overcome this problem, we used a "large eddy" method to directly approximate the dissipation rate from the dissipation rate ε_{SGS} at the resolved scale, which lies in inertial subrange (Sheng et al. 1998):

$$\varepsilon \approx \varepsilon_{SGS} = -2\left\langle \overline{\tau}_{ij} \cdot \overline{S}_{ij} \right\rangle, \quad \dots\dots\dots\dots\dots (8)$$

where $\bar{\tau}_{ij}$ is sub-grid scale (SGS) stress which needs to be modeled, $\bar{S}_{ij}$ is strain rate tensor at the resolved scale. The resolved strain rate tensor is the instantaneous strain rate tensor calculated from PIV measurement,

$$\bar{S}_{ij} = \frac{1}{2}\left(\frac{\partial \bar{U}_i}{\partial x_j} + \frac{\partial \bar{U}_j}{\partial x_j}\right).$$

The Smagorinsky Model (Smagorinsky, 1963) is used in this study to model the SGS stress. In order to fully resolve the dissipation rate of this highly three-dimensional flow, the 3D strain rate tensor is needed. Due to the limitation of PIV technique, however, only planar 2-component velocity field can be obtained simultaneously, and hence, only four out of nine strain rate components can be obtained. Consequently, the strain rate along the tangential direction is not available from the experiment. However, it was found that an empirical factor of 9/5 can be applied to the resolved dissipation tensor (Sheng et al., 1998). To improve the approximation accuracy, we suggest:

a) Adopt a PIV technique with higher spatial resolution. In the current work, the PIV measurement resolution is about 5 mm. With a larger CCD camera sensor (or film) and a smaller IC size, spatial resolution of PIV measurement as fine as sub-millimeter is achievable.
b) Apply a 3D PIV technique, such as holographic PIV (Meng and Hussain, 1995), Particle Tracking Velocimetry (Guezennec et al., 1994), and stereoscopic PIV (Adrain et al., 1997), to obtain all three velocity components and preferably resolved in 3D space. However, these techniques need further improvement to provide the required spatial and temporal resolution for CFD validation.

CFD simulation

VESSEL GEOMETRY

We have performed CFD simulations for the flow geometry, as described in the previous section for the PIV data using the commercial CFD code, Fluent™. The simulations were conducted in a fixed frame without considering the moving boundaries, namely the impeller blades. The presence of blades was accounted for by prescribing the boundary conditions just below the impeller using experimental data. As turbulence closures, both the k-ε RNG model and the more computational intensive RSM model were used. Details on the implementation of these models in Fluent™ can be found in the user manual (Fluent 1995).

A body fitted curvilinear (BFC) cylindrical coordinate system was adopted for the CFD simulation. Since the baffles were located in a symmetrical fashion, only one quarter of the vessel volume needed to be simulated. A periodic boundary was specified in the tangential direction. The solution domain had dimensions of 0.14715 m, 0.2921 m and 1.5708 radians in radius, axial and tangential direction, respectively. The following boundary conditions were specified for the computation.

1. Periodic boundary conditions at 0 and 1.5708 radians.
2. Symmetry boundary conditions along the axis of the vessel.
3. The baffle was represented as a thin solid surface of width $T/12$ and located tangentially (0.7854 radians) at a distance of $T/72$ from the vessel surface.
4. There was no physical presence of the impeller in the flow.
5. The no-slip condition and a wall roughness of 10% were defined for all bounded wall.
6. The grid dimensions were set at 52 × 27 × 17 along axial, radial and tangential directions, respectively.

IMPELLER BOUNDARY CONDITIONS AND TWO GROUPS OF SIMULATIONS

The presence of impeller in the flow was simulated by prescribing the velocity, turbulent kinetic energy and dissipation rate below the impeller based on experimental data. We have employed two sets of experimental data: (1) The PIV data for the same geometry were used as the impeller boundary conditions. (2) In accordance with simulations by Bakker et al. (1996), re-scaled LDV data were used as impeller boundary conditions. These LDV data were taken for a different geometry and different flow conditions. The LDV experimental vessel was a 0.145 m (T) diameter tank with four baffles attached to the vessel wall. The impeller diameter (D) was a 0.05 m (D/T = 0.35) in diameter P-4 turbine, located at 0.069 m from the bottom (C/T = 0.46). Another major difference between the LDV and PIV experiments was the impeller rotation speed. In the LDV experiment, the impeller was operating at 500 rpm, resulting in a Reynolds number (based on impeller diameter) N_{Re} = 21 500, while in PIV they were 60 rpm and N_{Re} = 9 000, respectively. In applying the LDV data as impeller outflow boundary conditions ($\vec{V}$, k, ε), the data were normalized and re-scaled with impeller tip velocity and tank diameter, as done by Bakker et al. (1996).

For the purposes of this study, we have conducted two groups of simulations. The first (our primary group) consists of CFD simulations with the k-ε RNG model using PIV data at the impeller and, partially, re-scaled LDV measurement data as boundary conditions. Hereinafter, this is referred to as PIV boundary conditions. The CFD results obtained from this group were validated against the PIV data. The discrepancy between CFD predictions and experimental full-field data was assessed. Meanwhile, the effect of prescribing different boundary conditions was studied using these simulation results. The second group includes simulations by two different closures (k-ε RNG model and RSM) using re-scaled LDV data as boundary conditions (hereinafter referred to as LDV boundary conditions). The mean velocity fields and turbulence fields were compared with each other and against PIV data.

With the PIV boundary conditions, the prescribed parameters at the impeller boundary were taken from the PIV measurement with the correct flow geometry (except for the missing components). That is, the axial and radial velocities at the impeller boundary were taken directly from PIV measurement, while the tangential velocity, turbulence kinetic energy and dissipation rate at the impeller boundary were approximated from LDV data. After inspecting the normalized PIV and LDV data in the impeller outflow region, we found that the velocity values from LDV were one third higher than from PIV; hence boundary conditions from LDV were rescaled accordingly to fit the flow to be simulated. The tangential boundary conditions were obtained from re-scaled LDV data and reduced by one-third. In order to smooth out experimental errors, instead of prescribing point by point, the velocity boundary conditions were prescribed by a profile modeled as a second-order polynomial approximation of the PIV data just below the impeller. The first two terms, $\langle u'\ u'\rangle$ and $\langle v'\ v'\rangle$, in the turbulence kinetic energy, were obtained directly from PIV measurement. The third term, $\langle w' \, w' \rangle$, was obtained from 3-component LDV data, re-scaled by tip velocity and modified in the same fashion as the tangential velocity components. The dissipation rate at the impeller was obtained from LDV measurement and modified accordingly. By inspecting both the LDV and the PIV data of these two quantities (k and ε), we found that the measurements just below the impeller were nearly constant. Hence, to simplify the prescription procedure and to eliminate the effect of experimental errors on the simulation, constant values for these two quantities were prescribed as their impeller boundary conditions.

These boundary conditions are expected to introduce errors into simulation results due to the empirical prescription of turbulent kinetic energy and turbulence dissipation rate. However, these effects on the mean velocity flow pattern simulation by k-ε RNG model were found to be insignificant. This insensitivity of the mean flow was also reported by Fokema et al. (1994). In order to verify this conclusion on the particular stirred vessel flow simulation by k-ε RNG model, three more simulations were conducted based on the same velocity boundary conditions by varying k and ε from 20% higher to 20% lower than their original values. The mean flow velocity did not exhibit any changes except for magnitude variation of ±5%. Hence, as a first-order approximation, k and ε were prescribed as constants at the impeller. Table 1 summarizes the boundary conditions for the first simulation group.

In the second simulation group, the same boundary conditions as described by Bakker et al. (1996) were adopted (i.e., based entirely on re-scaled LDV data acquired for a different impeller flow.) Hereinafter, this is referred to as LDV boundary conditions. Table 2 shows the LDV boundary conditions used for this simulation group. Comparing the simulation results, we have examined the effect of various boundary conditions on the CFD predictions.

Comparison tools for spatial distributions

To validate CFD results against PIV data, tools for quantitative comparison between two sets of 2D flow fields are needed. Let us consider a pair of 2D scalar fields $S_1(x,y)$ and $S_2(x,y)$. A set of parameters are introduced to address the following questions:

(1) How can we determine the discrepancy between the compared quantities?
(2) How can we quantify the similarity of the two compared quantities with respect to space?
(3) How can we quantify the discrepancy and similarity evaluated within a certain length scale and to provide either a global or local view of them?

SPATIAL SPECTRUM

The spatial spectrum of a field, $S(x,y)$, is defined as

TABLE 1
PIV Boundary Conditions: Radial and axial velocities are prescribed by fitted PIV data. Other impeller outflow boundary conditions are normalized and rescaled from LDV measurements of a 5" vessel

Radial velocity (U)	$-77.7453 \cdot x^2 + 4.5417 \cdot x - 0.0126$ (m/s)
Axial velocity (V)	$16.886 \cdot x^2 - 0.42322 \cdot x + 0.0038$ (m/s)
Circumferential velocity (W)	$-51.8302 \cdot x^2 + 3.0278 \cdot x^2 - 0.0084$ (m/s)
Kinetic energy (k)	2.2×10^{-3} (m^2/s^2)
Dissipation rate (ε)	4.0×10^{-2} (m^2/s^3)

$$\tilde{S}\left(f_x, f_y\right) = \int\int S(x,y) \cdot e^{-2\pi j(f_x \cdot x + f_y \cdot y)} dxdy, \quad \ldots\ldots\ldots \quad (9)$$

where f_x, f_y are spatial frequencies (wave numbers) of the signal along x and y directions. The spectrum analysis can provide characteristics of the spatial variation of the fields. When $S(x, y)$ is the mean velocity field, we can relate the wave numbers to the inverse of recirculation-zone sizes and the velocity spectrum to the velocity distribution in zones of different scales. Computing signal spectra is rather simple, but they provide a better view of amount of discrepancy between compared fields (e.g. the simulated and experimental data) than the original fields themselves.

CORRELATION

A modified correlation coefficient of two fields, V_{12}, can be used to quantify the similarity between two fields $S_1(x, y)$ and $S_2(x, y)$. It is a scalar quantity defined as

$$V_{12} = \frac{\iint_A S_1(x,y) \cdot S_2(x,y) dxdy}{\sqrt{\iint_A [S_1(x,y)]^2 dxdy \cdot \iint_A [S_2(x,y)]^2 dxdy}}, \quad \ldots\ldots\ldots \quad (10)$$

where A is the area of the entire domain. It is easy to see that V_{12} is equal to the cross-correlation coefficient valued at zero shifts. Let $R_{12}(\tau_x, \tau_y)$ represent the cross-correlation function between S_1 and S_2; then

$$V_{12} = \left. \frac{R_{12}\left(\tau_x, \tau_y\right)}{\sqrt{R_{11}\left(\tau_x, \tau_y\right) \cdot R_{22}\left(\tau_x, \tau_y\right)}} \right|_{\substack{\tau_x = 0 \\ \tau_y = 0}}, \quad \ldots\ldots\ldots \quad (11)$$

where R_{11}, R_{22} are auto-correlation functions with respect to space. The value range of V_{12} varies from –1 to 1, with 1 representing the maximum similarity between the fields and –1 representing the maximum similarity with opposite valuation of the fields.

TABLE 2
LDV Boundary Conditions: LDV measurement for a 5" vessel is normalized, re-scaled, and prescribed as impeller outflow boundaries

Radius/T	U (m/s)	V (m/s)	W (m/s)	k (m^2/s^2)	ε (m^2/s^3)
0.0267	1.09×10^{-2}	2.19×10^{-3}	8.27×10^{-3}	1.11×10^{-3}	7.24×10^{-3}
0.0366	1.67×10^{-2}	3.38×10^{-3}	1.21×10^{-2}	1.11×10^{-3}	7.24×10^{-3}
0.0565	2.56×10^{-2}	5.17×10^{-3}	1.79×10^{-2}	1.11×10^{-3}	7.24×10^{-3}
0.0764	4.60×10^{-2}	7.44×10^{-3}	3.46×10^{-2}	1.24×10^{-3}	8.55×10^{-3}
0.0962	7.42×10^{-2}	1.03×10^{-2}	4.83×10^{-2}	1.24×10^{-3}	8.58×10^{-3}
0.1161	9.54×10^{-2}	1.16×10^{-2}	5.66×10^{-2}	1.23×10^{-3}	8.54×10^{-3}
0.1359	1.12×10^{-1}	1.15×10^{-2}	6.48×10^{-2}	1.58×10^{-3}	1.24×10^{-3}
0.1558	1.26×10^{-1}	1.47×10^{-2}	7.82×10^{-2}	2.95×10^{-3}	3.16×10^{-2}
0.1757	9.17×10^{-2}	1.99×10^{-2}	8.56×10^{-2}	6.10×10^{-3}	9.39×10^{-2}

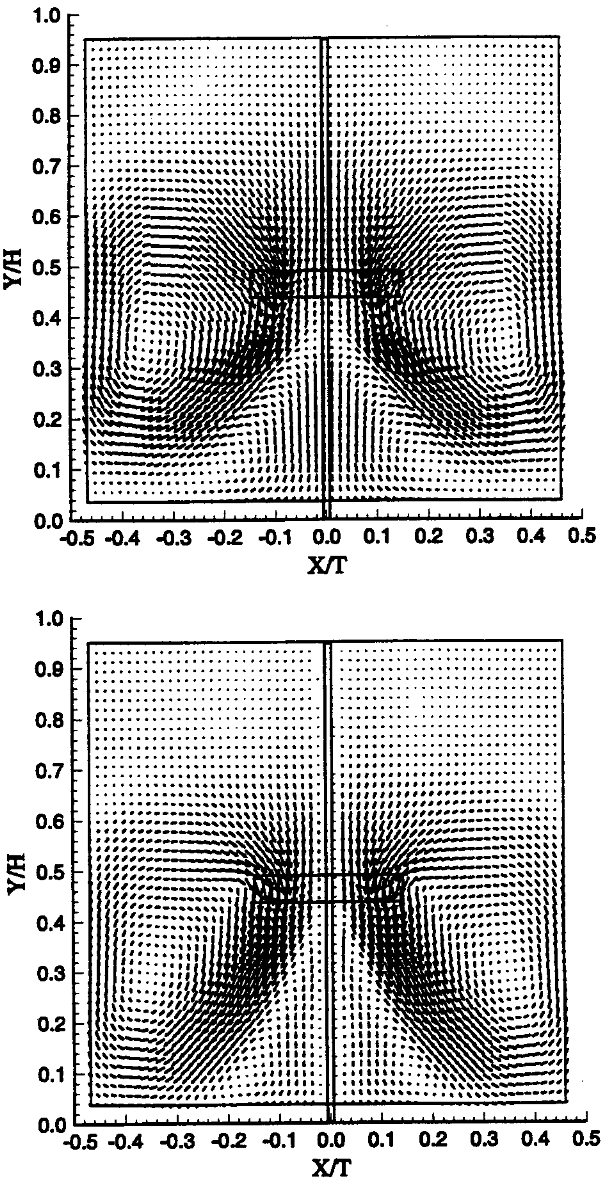

Figure 2 — Mean velocity field. Top: PIV (after mirroring). Bottom: CFD with k-ε RNG model and PIV boundary conditions.

LOCAL CORRELATION

The methods described above can help us to get a global view of the similarity and discrepancy between the experimental and simulation data. However, these techniques are not suitable for comparing the data locally. The direct pointwise or normalized error surface can be used to get some information about the local discrepancy or similarity between data, but the choice of the quantity to be used as the denominator for normalization is not easy. The use of either experimental measurement or CFD simulations will result in the magnification of the error.

In order to get a better local comparison, a quantity known as local correlation is used. It is defined as

$$Corr(x_0,y_0,\delta)=\frac{\iint\limits_{A(x_0,y_0,\delta)} S_1(x,y)\cdot S_2(x,y)dxdy}{\iint\limits_{A(x_0,y_0,\delta)}[S_1(x,y)]^2dxdy\cdot\iint\limits_{A(x_0,y_0,\delta)}[S_2(x,y)]^2dxdy}, \quad (12)$$

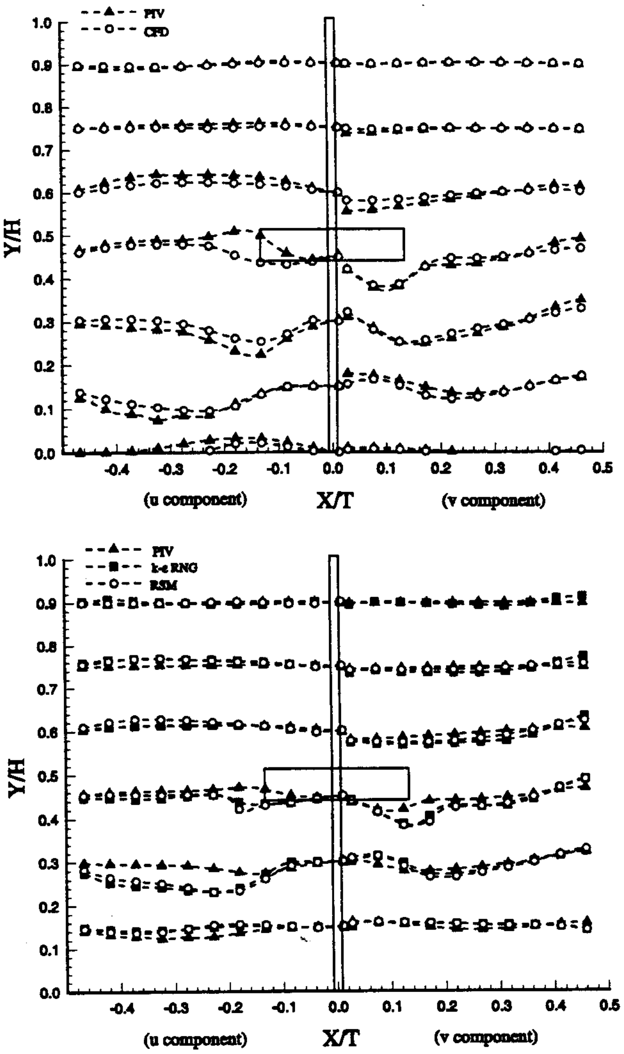

Figure 3 — Comparison of experimental and predicted velocity profiles at different heights from the vessel bottom. Top: PIV boundary conditions. Bottom: LDV boundary conditions. Left: Radial velocity component, u. Right: Axial velocity component, v.

where $A(x_0, y_0, \delta)$ is a local comparison area with the origin at (x_0, y_0) and has a length scale of δ. This quantity gives the similarity of the fields within a small region, and since it is normalized by DC power of each field, it is not affected by the bias mentioned earlier. By varying the length scale, δ, the fields are compared at different local sizes. However, it is to be noted that any discrepancies whose length scales are smaller than δ will be smoothed out. It is found that when the size of the smallest recirculation zone visible (the secondary vortex at the bottom of the vessel, Figure 2 top) is chosen as the length scale, the local correlation distribution is much smoother, sharper and clearer. This length scale is hence used in this study.

Results and discussion

ON CFD SIMULATION WITH PIV BOUNDARY CONDITIONS

In this section, results from a validation study of CFD simulations with the k-ε RNG model using the PIV boundary conditions (Table 1) are reported. These boundary conditions are largely taken from the PIV measurement of a flow with the exact geometry and N_{Re}. The mean velocity

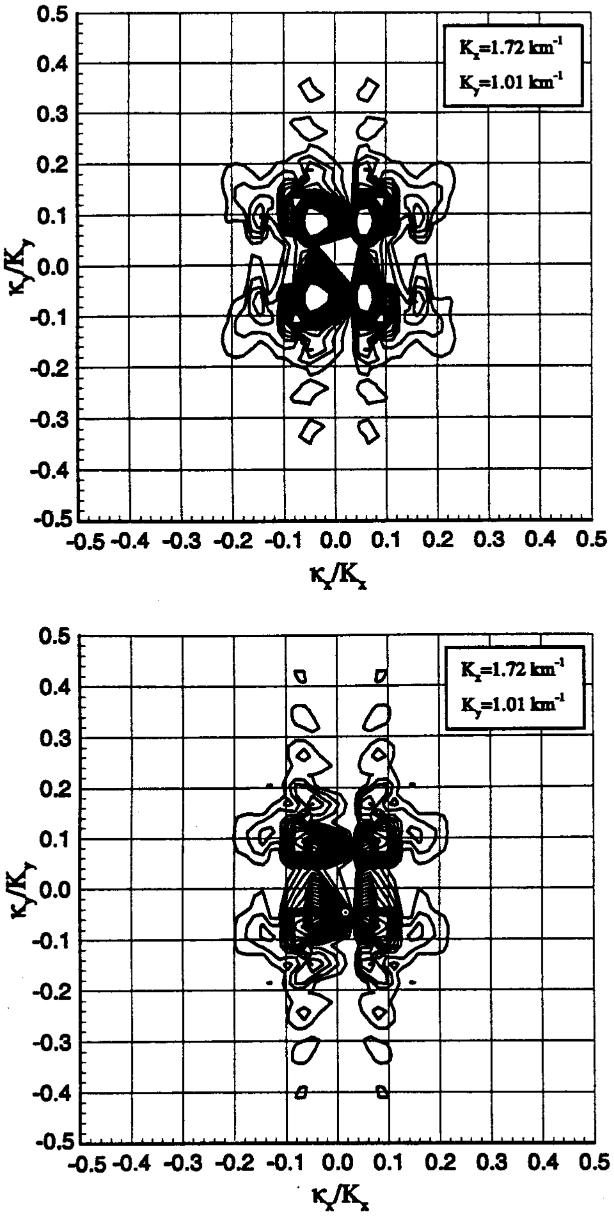

Figure 4 — Spatial power spectra of radial mean velocity component, u. Top: PIV. Bottom: CFD with k-ε RNG model and PIV boundary conditions.

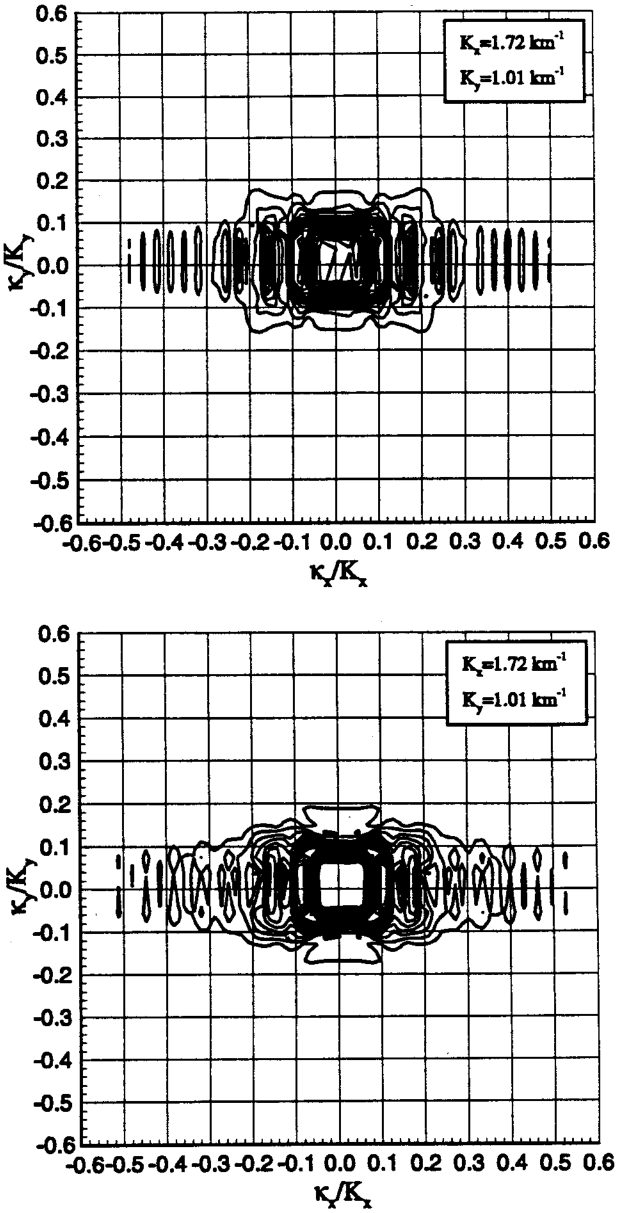

Figure 5 — Spatial power spectra of axial mean velocity component, v. Top: PIV. Bottom: CFD with k-ε RNG model and PIV boundary conditions.

field, flow pattern, Reynolds stresses, turbulent kinetic energy, and turbulence dissipation rate were compared quantitatively. Since the Reynolds shear stresses at the impeller boundary could not be extracted from PIV data completely, CFD predictions using the RSM are not reported.

Mean Velocity Field

Figure 2 (top and bottom) shows the mean velocity fields obtained from the PIV (after mirroring) and CFD. Their similarities have been investigated both qualitatively and quantitatively with the tools introduced above. Both clearly show two counter-rotating vortices in the mean flow and a distinct shear layer between the two vortices. The locations of the vortex cores match closely with each other. Their coordinates are (0.14, 0.32) from PIV vs (0.14, 0.30) from CFD for the first vortex and (0.30, 0.08) from PIV vs (0.34, 0.08) from CFD for the second. The differences are within ± 5%. To further examine the degree of match in each velocity component, we have plotted the radial velocity, u, and axial velocity, v, as a function of radius at several heights from the vessel bottom (Figure 3-top). It is observed that the axial component (v) predicted by CFD matches with PIV within ± 10%. In the impeller and flow discharge region, the error reduces to ± 5%. The radial component (u) shows good agreement in the upper part of the stirred vessel, but large uncertainties are found in the flow discharge region, near the tip of the impeller, and in the flow return region right above the impeller tip. By examining the spatial spectra of the radial and axial velocity components (Figures 4 and 5), we found that large-scale motions, represented by the smaller wavenumber components towards the center in the spectra, match reasonably well. The peaks near the spectrum center can be identified with the largest structures in the mean velocity field. In particular, they are contributed by the pair of the main recirculation zones generated by the impeller and a

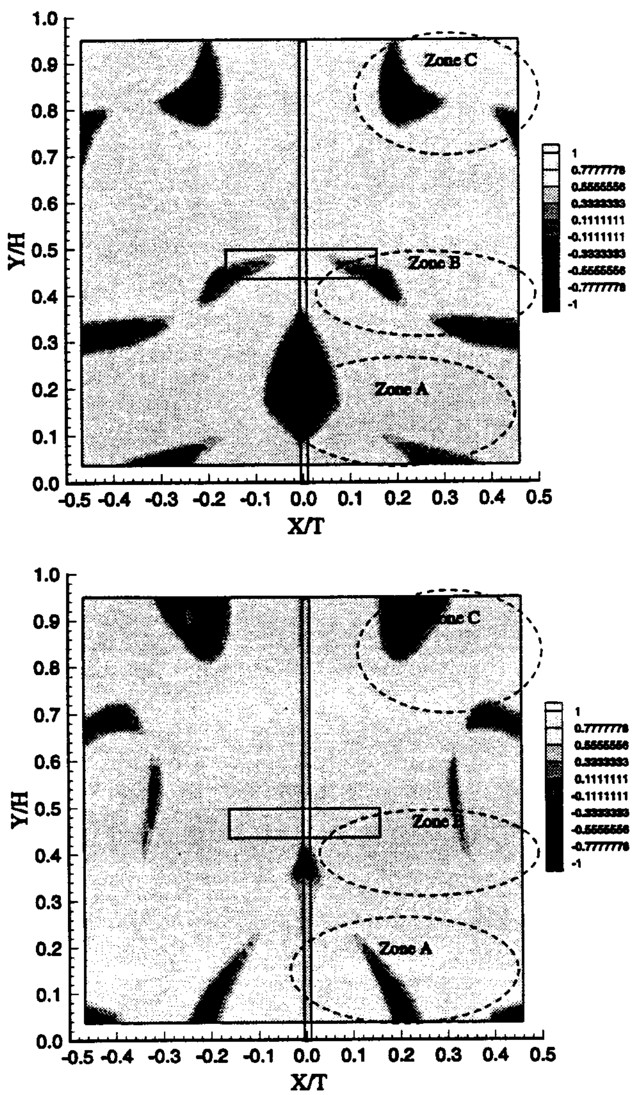

Figure 6 — Local correlation of PIV and CFD. Top: Radial velocity component, u. Bottom: Axial velocity component, v.

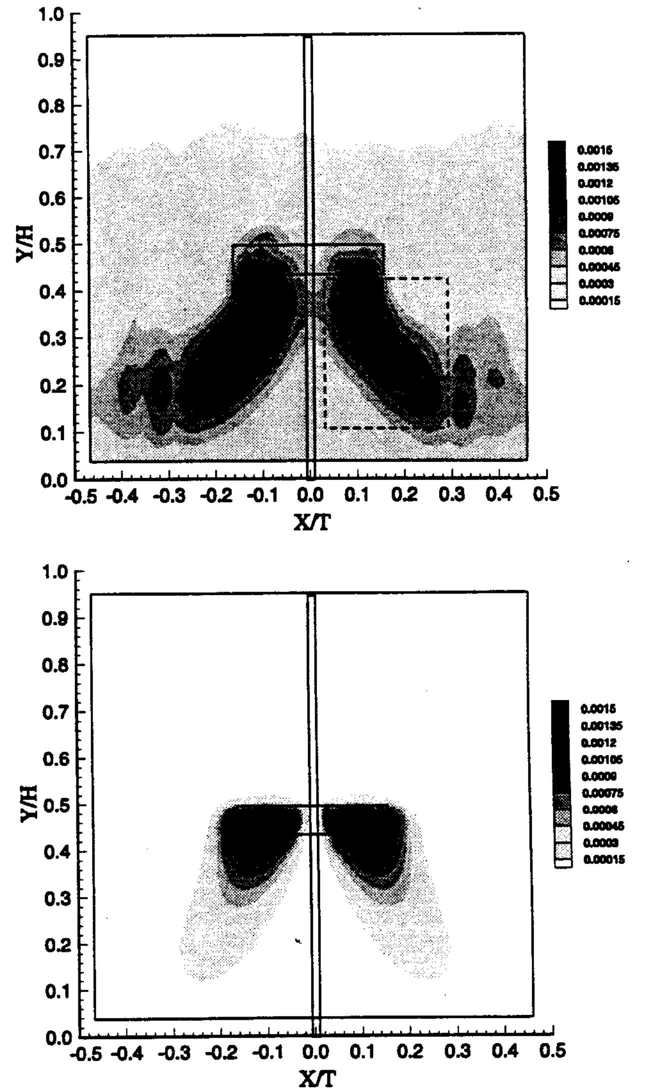

Figure 7 — Turbulent kinetic energy distribution. Top: PIV. Bottom: CFD with k-ε RNG model and PIV boundary conditions.

pair of smaller recirculation zones near the shaft and the vessel bottom. Hence, the CFD simulations captured the main characteristics of the mean flow pattern.

However, the CFD prediction does exhibit some notable discrepancies with the PIV. From the mean velocity field (Figure 2), the flow discharge angle was 30° for CFD, compared with 45° for PIV. This suggests that in the simulated flow the discharged fluid loses its vertical momentum slower and is less inclined to move towards the vessel wall than in the real flow. This deeper discharge results in more abrupt turnings in the predicted flow pattern. From the mean velocity spatial spectra, we observe high wave number components along the axial direction for the radial component (Figure 4), which correspond to a sharp turning of the mean flow in the region above the impeller, and those along radial direction for the axial component (Figure 5), which correspond to the

TABLE 3

Comparison of Major Features of Mean Flow Patterns from PIV Data and CFD Simulation with k-ε RNG Model and PIV Boundary Conditions. The relative discrepancy reported in the final three rows is measured with respect to PIV results

	PIV	CFD
Flow discharge angle	45°	30°
Location of 1st vortex	(0.14, 0.32)	(0.14, 0.32)
Location of 2nd vortex	(0.30, 0.08)	(0.34, 0.08)
Cutoff wavenumber for radial component	κ_x cutoff = 450 m^{-1} κ_y cutoff = 320 m^{-1}	κ_x cutoff = 430 m^{-1} κ_y cutoff = 400 m^{-1}
Cutoff wavenumber for axial component	κ_x cutoff = 820 m^{-1} κ_y cutoff = 160 m^{-1}	κ_x cutoff = 860 m^{-1} κ_y cutoff = 160 m^{-1}
Large discrepancy regions	1. Flow separation (70%) 2. Trailing vortices (30%~70%) 3. Top swirling flow (70%)	

sharp turning at the bottom of the stirred vessel. Evidently these turnings were sharper for CFD than for PIV.

Correlation distributions of radial and axial velocity components (Figure 6) show three zones of large prediction discrepancies between CFD and PIV, as marked by A, B, and C. Zone A is associated with a high-shear layer. Zone B, which extends from the tip of impeller to the vessel wall, might be related to the tip trailing vortices (Calabrese and Stoots 1989). Zone C , near the top, contains weak azimuthal motion not shown in the 2D plane. These three regions are separated by two regions where CFD and PIV match very well with high correlation values. The poor prediction accuracy of the mean flow in the three zones can be related to turbulence model deficiencies. In Zone A (high-shear layer), the k-ε model underpredicts the Reynolds stresses which results in an increased mean velocity in CFD. In Zone B, the presence of tip trailing vortices is likely to make the isotropy assumption that is implicit in the k-ε model invalid. In Zone C, the prediction uncertainty may be attributed to the lack of prescription of boundary conditions at the free surface as well as the inaccuracy of the k-ε model at low Reynolds numbers. In addition, near the low part of the shaft, there is a region of large discrepancy,.which can be attributed to the absence of the shaft in the CFD simulation.

In general, the CFD simulation based on k-ε model predicts the mean flow pattern rather well. Table 3 highlights the major features of CFD and PIV results.

Turbulent kinetic energy

In Figure 7, we present the distributions of the turbulent kinetic energy from PIV and CFD. These distributions appear qualitatively similar. Both show an impeller region with highly concentrated k, the magnitude of which decreases as the mean flow field is discharged downward to the bottom. The magnitudes near the impeller region and flow discharge region agree reasonably well (within ± 5% and ± 10% error). By integrating k over the entire center plane, we obtain 0.36 J/kg from CFD and 1.55 J/kg from PIV. Hence, CFD underpredicts the turbulent kinetic energy in the entire vessel. By integrating k over two sub-regions in the flow field, we found that CFD correctly predicts k in the impeller region, i.e. half of the area enclosed by the solid line (0.15 J/kg compared with 0.19 J/kg in PIV), but underpredicts k by a factor of four in the flow discharge region, enclosed by the dash line (0.13 J/kg vs 0.54 J/kg).

Turbulence dissipation rate

The turbulence dissipation rate was estimated from the experiment by a large eddy PIV method proposed by Sheng et al. (1998). Figure 8 shows the experiment-estimated and CFD-predicted dissipation rate. Both show a highly dissipative impeller region and a decrease of the dissipation rate magnitude following the downward discharge of the mean flow. The predicted average dissipation rate in the impeller region is close to that from PIV (2.3 m^2/s^3 from CFD vs 2.5 m^2/s^3 from PIV). However, CFD underpredicts the dissipation rate in the flow discharge region by four folds (1.1 m^2/s^3 compared with 3.9 m^2/s^3 in PIV). Examining the relative average dissipation rate (normalized with total dissipation rate of the entire vessel), we see from the CFD prediction that 63% of the total TKE is dissipated in the impeller region, only 29% is dissipated in the flow discharge region, and 10% in the rest of the tank. In contrast, the PIV results show that 30% turbulent kinetic energy is dissipated in the impeller region, 50% in the discharge region, and 20% in the rest of the tank. Hence, the CFD prediction focuses more dissipation near the impeller.

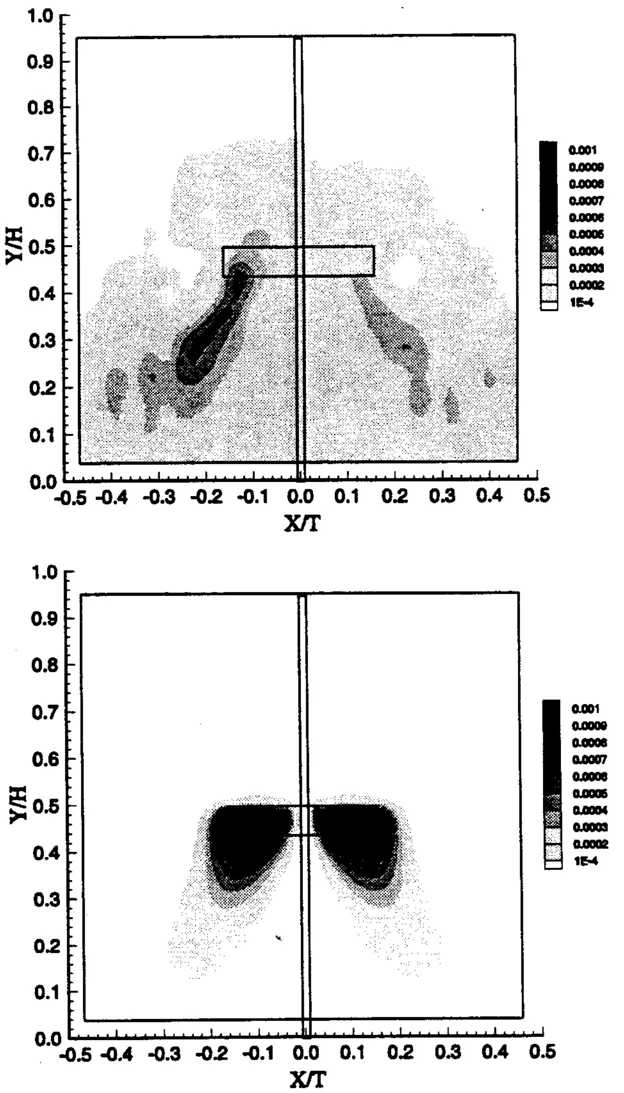

Figure 8 — Turbulence dissipation rate normalized with N^3D^2. Top: Estimated from PIV measurement. Bottom: k-ε RNG model with PIV boundary conditions.

Reynolds stresses

Reynolds stresses are the unclosed terms in the RANS equation which need to be modeled. Figures 9 and 10 show the distributions of some Reynolds stress terms from PIV and CFD. Since the CFD simulation based on the k-ε model does not predict the cross terms (Reynolds shear stresses), we only compare the two normal stresses, $\langle u'^2 \rangle$ and $\langle v'^2 \rangle$, and leave the validation of cross terms to the next section, where the RSM is discussed. It is worthwhile to mention that in the experiment the cross term $\langle u' \, v' \rangle$ has the same magnitude as normal stresses, while in the CFD prediction based on k-ε RNG model, if we estimate the cross term by Boussinesque hypothesis, $\langle u' \, v' \rangle$ is at least one order of magnitude smaller than normal stresses and significantly smaller in the flow discharge region.

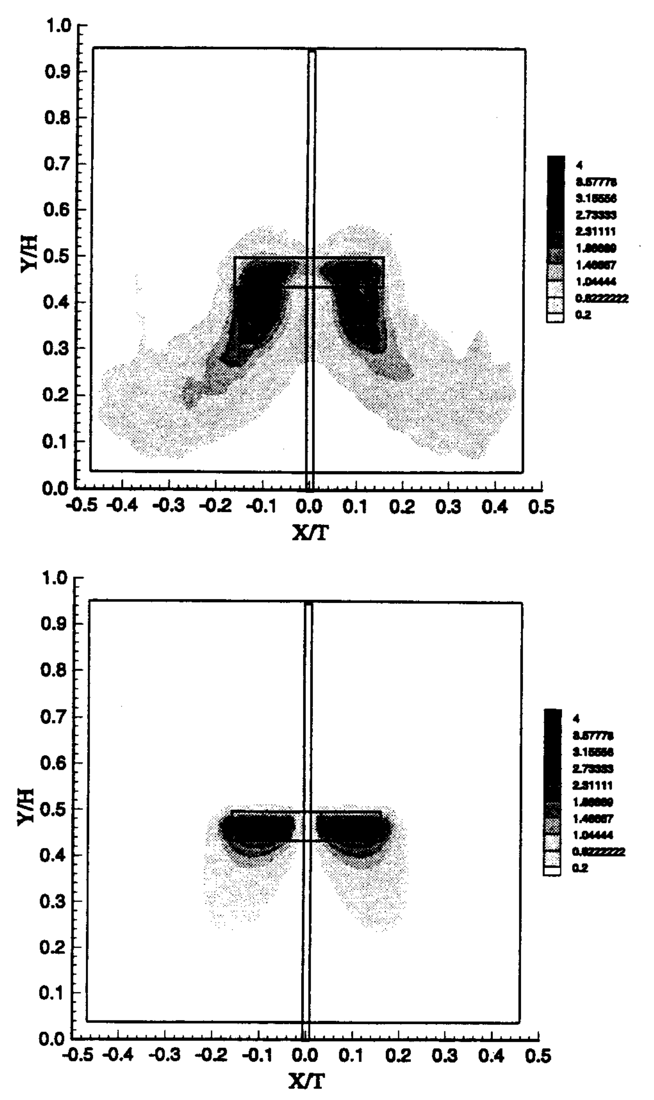

Figure 9 — Normal stress $\langle u'^2 \rangle$. Top: PIV. Bottom k-ε RNG model with PIV boundary conditions.

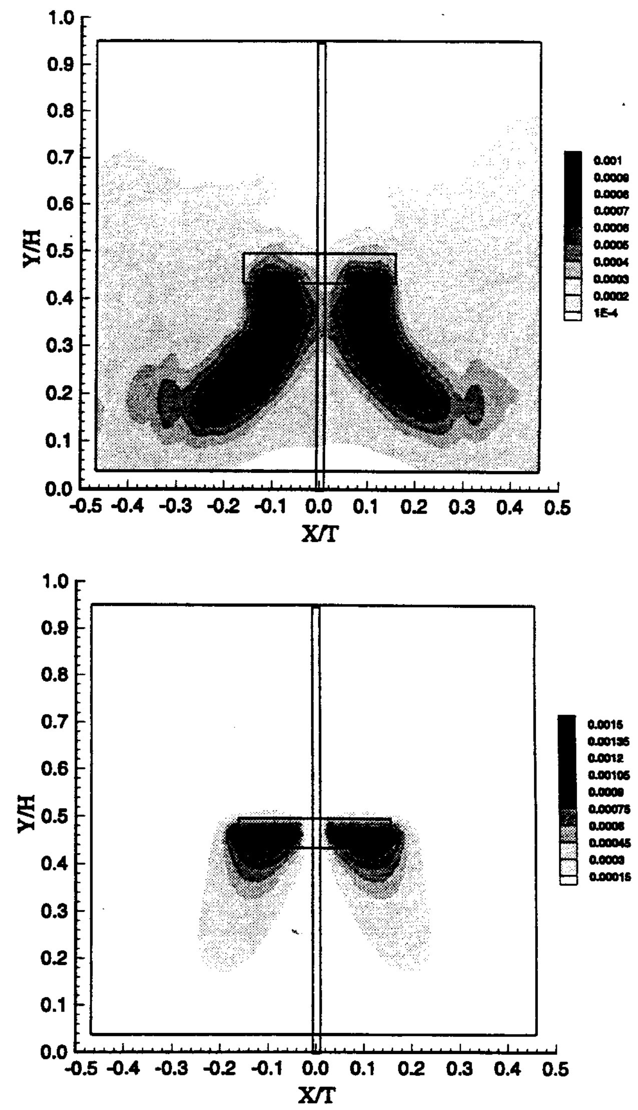

Figure 10 — Normal stress $\langle v'^2 \rangle$. Top: PIV. Bottom: k-ε RNG model with PIV boundary conditions.

All the turbulence quantities examined including $\langle u'^2 \rangle$ in Figure 9 and $\langle v'^2 \rangle$ in Figure 10 show consistent underprediction in the flow discharge region. To obtain insight into this underprediction, it is helpful to take a look at PIV measurements of instantaneous velocity fields. Figure 11 shows four randomly picked PIV snapshots with the instantaneous velocity field superposed by its vorticity field. It is clear from these pictures that flow in the discharge region contains a large number of time-varying eddies of different sizes and hence is a source of turbulence kinetic energy production. Inability of the model to describe this complex flow may lead to large discrepancies in the Reynolds stresses, turbulent kinetic energy, and dissipation rate.

In general, we have found that the k-ε RNG model predicts the mean velocity field reasonably well. Correctly prescribed PIV boundary conditions at the impeller can lead to rather accurate overall prediction of mean flow pattern for this fairly complex flow without sliding mesh and/or time-dependent CFD (Bakker et al. 1996). However, relatively large uncertainties of mean velocity field are found in the high shear regions, the trailing vortex sweeping region and the low Reynolds number swirling flow region in the top of the vessel. Regarding the turbulent parameter fields, CFD can qualitatively predict the distribution of the kinetic energy, turbulence dissipation rate, and normal Reynolds stresses to some extent. The predictions of these quantities in the impeller region agree with PIV rather well. However, it is apparent that the k-ε RNG simulation underpredicts k, ε, and normal Reynolds stresses in the flow discharge region which, as seen in time-resolved instantaneous measurement, contains a large number of different-size eddies. In this region the local isotropic assumption used in k-ε model does not hold.

ON CFD SIMULATION WITH LDV BOUNDARY CONDITIONS

In this section, we discuss CFD results from the second simulation group using LDV boundary conditions (Table 2). These boundary conditions were taken from a measurement of a flow with different geometry, rescaled with tip velocity and tank diameter. CFD predictions by two closures for Reynolds stresses, namely k-ε RNG and RSM, are compared with each other. Since the LDV boundary conditions (based entirely on rescaled LDV data by Bakker et al. 1996, N_{Re} = 21 500) are inconsistent with the current PIV data (N_{Re} = 9 000), only qualitative comparisons are emphasized

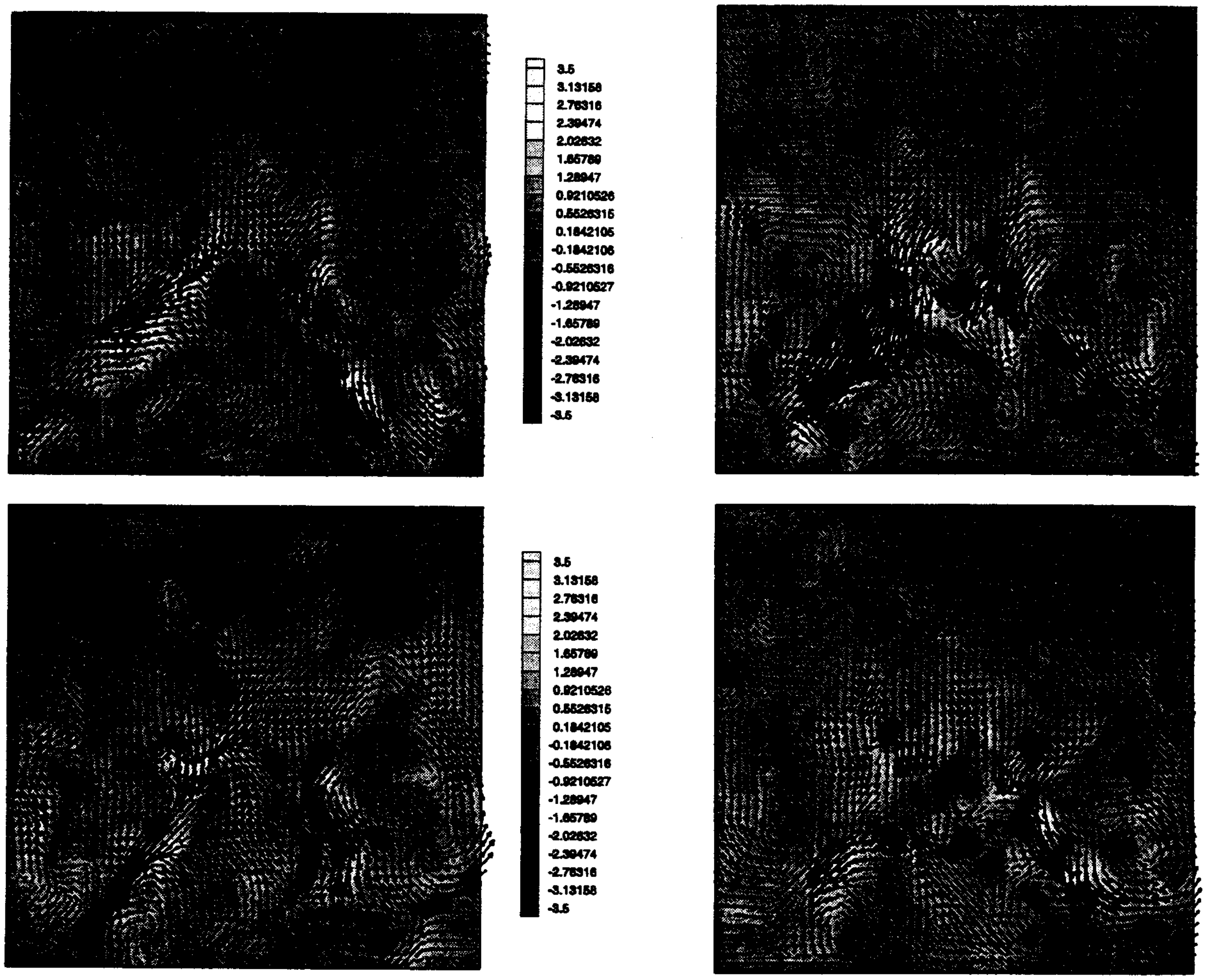

Figure 11 — Four consecutive instantaneous 2D PIV velocity fields acquired by PIV, sub-sampled every 16.6 s, superposed with out-of-plane vorticity magnitude (represented by grey level).

when assessing the effects of different closures using PIV experimental results.

Mean velocity field

Figure 12 shows the mean velocity predicted by the k-ε RNG model and by RSM. They are very similar to each other, and both predict the two counter rotating recirculation patterns in the entire tank. However, the locations of the two vortices are higher than in PIV. It is interesting to notice from Figure 12 the obvious difference between the k-ε RNG model with the LDV boundary conditions (top) and the PIV boundary conditions (bottom).

The influence of boundary conditions can be examined as follows. With the PIV boundary conditions, the primary vortical structure occupies nearly the entire region below the impeller, whereas with the LDV boundary conditions, the structure is concentrated near the center of the vessel. Also the secondary vortex seems to be shifted away from the shaft side to the vessel wall side. Moreover, the results with PIV boundary conditions show strong recirculation above impeller. On the other hand, with the LDV boundary conditions only the fluid close to impeller top region is moving towards the impeller. Recall that the primary difference between the PIV and LDV boundary conditions resides in the geometric and dynamic flow conditions. Thus, accurate boundary conditions obtained from experimental models bearing both geometric and dynamic similarity with the simulated flow are required to correctly predict the mean flow. This also suggests that the simple scale-up rules such as scaling by tip velocity widely used for stirred vessel CFD is insufficient for predicting the correct mean velocity field. To achieve dynamic similarity, the Reynolds number N_{Re} must be kept the same during scaling.

Finally, in Figure 3 (bottom), we plot the radial and axial components, u and v, of the two CFD simulations with LDV boundary conditions and PIV measurements at different off-bottom distances. Consistency in the mean velocity field predictions from k-ε RNG model and RSM is evident. We can also see that, compared with PIV, both models predict the velocity in the upper part of the vessel rather well, but poorly in the lower part of vessel, especially at the tip of the impeller and the bulk of discharge flow. The error, we believe, mainly comes from the incorrect boundary conditions (LDV boundary conditions).

Evidently, CFD simulations are very sensitive to boundary conditions, and the use of re-scaled LDV data from a different stirred vessel geometry exerts a strong influence on the simulation results. This strong influence is already manifested in the predicted mean flow field. Since the results indicate that the mean velocity field prediction tends to have the least discrepancies with experimental data, greater uncertainties can be expected in other flow quantities (k, ε, Reynolds stresses). We have also found that in prescribing

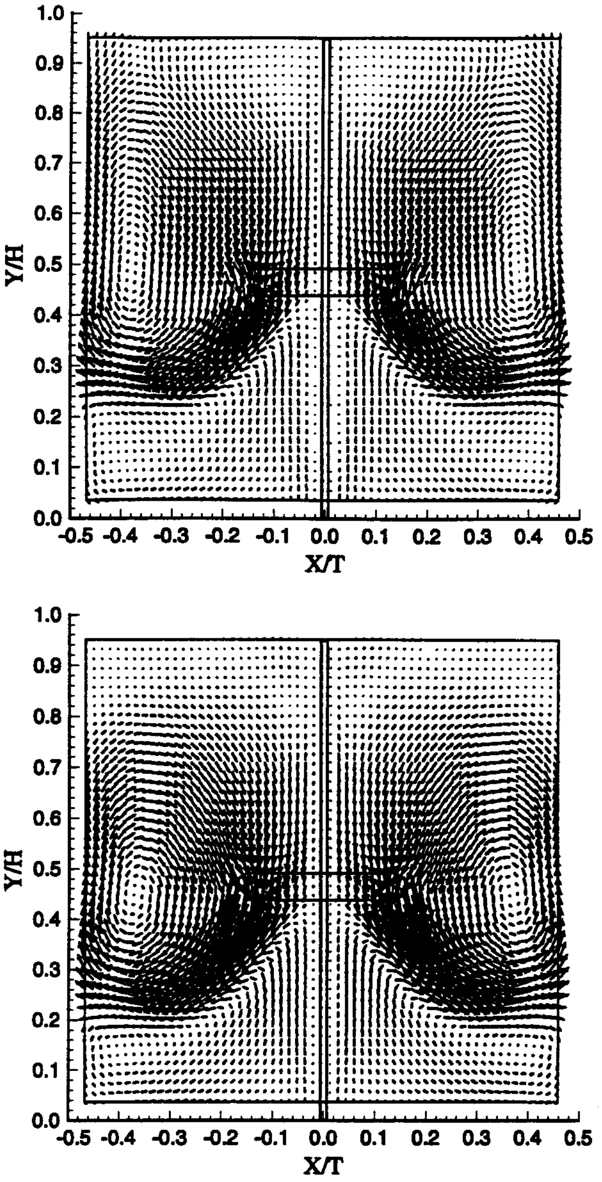

Figure 12 — Mean velocity predicted field by CFD using LDV boundary conditions. Top: k-ε RNG model. Bottom: RSM.

the boundary conditions it is most important to have the mean velocity data from the correct flow geometry. The kinetic energy and dissipation rate prescriptions, on the other hand, play a less crucial role in determining the mean flow field. For example, varying the prescribed kinetic energy and dissipation rate values in the PIV boundary conditions by ± 20%, the simulated mean flow field showed no significant changes.

Turbulent kinetic energy

Figures 13 shows the turbulent kinetic energy distributions obtained from CFD using the k-ε RNG model and RSM. Both predict a highly concentrated kinetic energy at the impeller tip. However, compared with experimental results, both models underpredict k by one order of magnitude (0.17 J/kg for the k-ε RNG model, 0.40 J/kg for RSM, compared with 1.6 J/kg for PIV). In the impeller region, the predicted total kinetic energies roughly match with PIV (0.11 J/kg, 0.17 J/kg, and 0.19 J/kg, respectively), but in the flow discharge region they are underpredicted by one order of magnitude (0.04 J/kg, 0.08 J/kg, and 0.54 J/kg). It is also evident that RSM does predict a relatively high k region, which corresponds to the flow discharge region in the mean flow field, but the magnitude of this region is far less than seen with PIV. This difference between RSM and the k-ε RNG model may suggest that RSM is better in simulating turbulence fields in high shear regions.

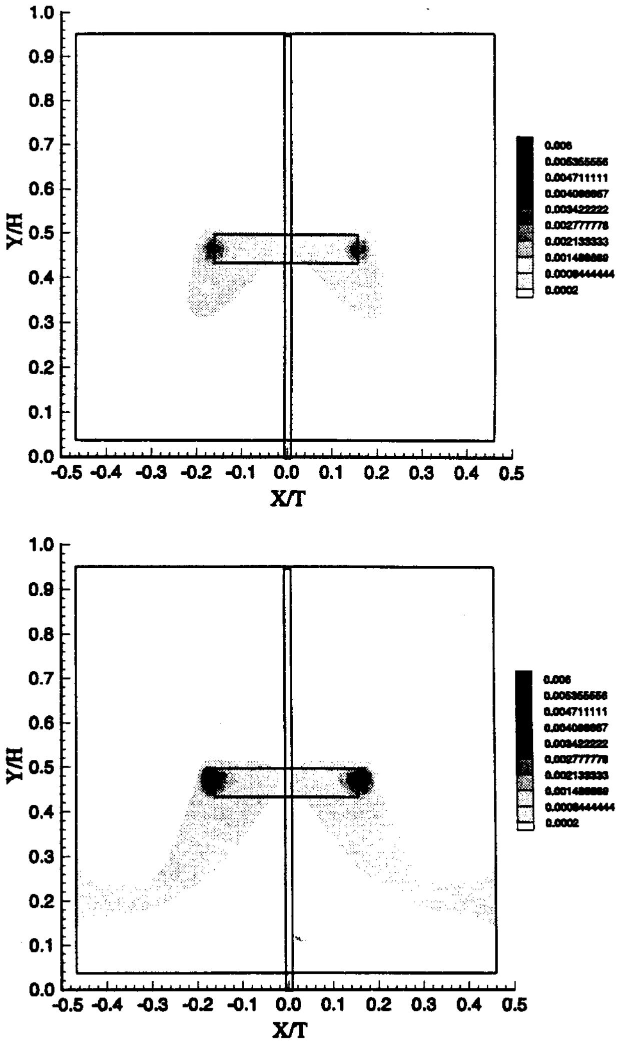

Figure 13 — Turbulent kinetic energy predicted by CFD with LDV boundary conditions. Top: k-ε RNG model. Bottom: RSM.

Turbulence dissipation rate

Turbulence dissipation rate fields, predicted by the k-ε RNG model and RSM (Figure 14) show rather good agreement with each other. The simulations show that turbulent kinetic energy has the largest dissipation rate at the impeller tip. The distributions of dissipation rate matches their turbulent kinetic energy distributions rather well. By integrating the dissipation rate over the impeller region and flow discharge region, we found that they both give similar predictions of dissipation rate in these regions, 80% in impeller region and 10% in the flow discharge region. Compared with PIV (consistent with the average dissipation rate reported by Wu and Petterson 1989; Jaworski and Fort 1991), which is 30% in the impeller region and 50% in the flow discharge region, CFD predicts much lower values in the flow discharge

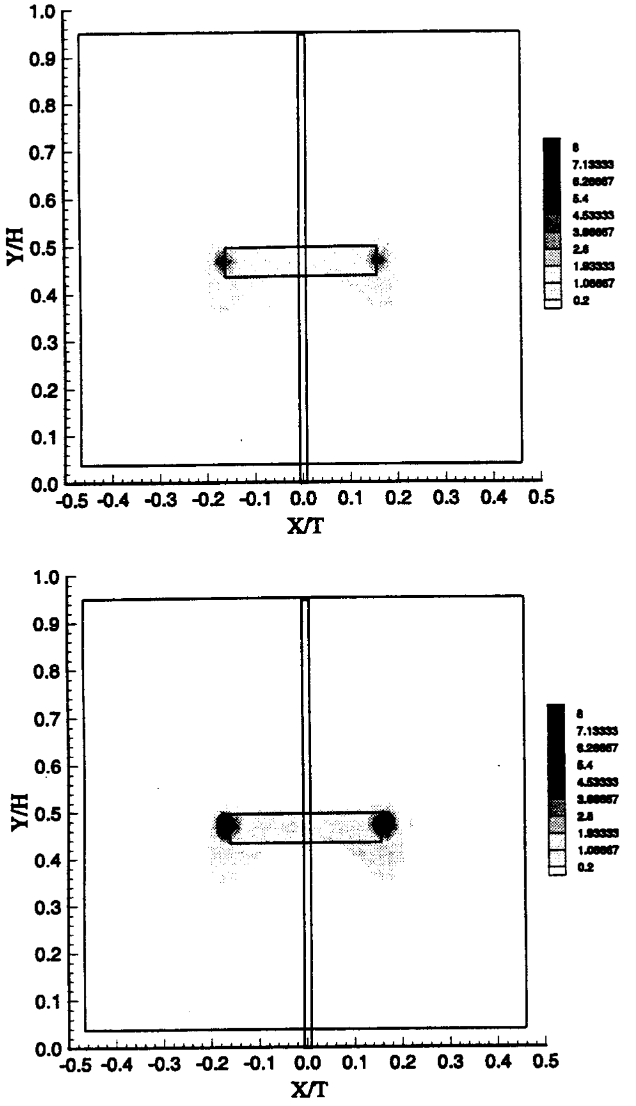

Figure 14 — Turbulence dissipation rate predicted by CFD with LDV boundary conditions (normalized with N^3D^2). Top: *k*-ε RNG model. Bottom: RSM.

region. Therefore, we may conclude that CFD, regardless of the turbulence model used, tends to underpredict ε in the flow discharge region. In contrast to *k*-ε RNG model, RSM does show a flow discharge region with high dissipation rate values while the magnitude is much smaller. Moreover, both CFD models show less homogeneous distributions than PIV. Represented by the maximum to minimum ratio, the inhomogeneity is found to be 30 for both the *k*-ε RNG model and RSM, and 10 for PIV.

Reynolds stresses

Figure 15 shows a comparison of the distributions for Reynolds shear stress, $\langle u'\ v' \rangle$, predicted by RSM and measured by PIV. Similar to the experimental result, RSM predicts a high Reynolds stress region extending from impeller to the vessel wall, which corresponds to the flow discharge region with time-varying eddies. The shape of this region, however, differs from PIV. It is also noticed that the values of the predicted Reynolds shear stress are one order of magnitude smaller than for PIV. Figure 16 presents the normal stresses $\langle u'^2 \rangle$ and $\langle v'^2 \rangle$ simulated by RSM, which evidently show the same characteristics as the Reynolds shear stress. However, they are two orders of magnitude higher than the simulated $\langle u'\ v' \rangle$, while for PIV all the stresses have the same order of magnitude. This indicates that the real flow is much more anisotropic than predicted by RSM.

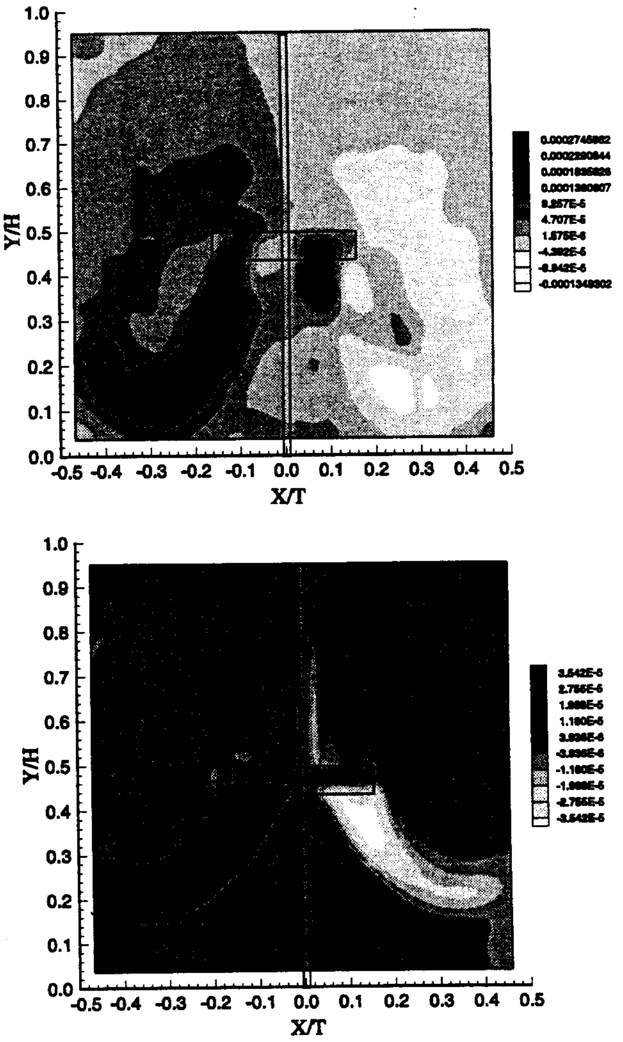

Figure 15 — Reynolds shear stress $\langle u'v' \rangle$. Top: PIV. Bottom: RSM using LDV boundary conditions.

From the comparisons above, we conclude that although there is no major difference in the mean flow patterns predicted by the *k*-ε RNG model and RSM, the differences in turbulence fields predicted by them are rather significant, especially for the Reynolds shear stress and the turbulence kinetic energy. Both models appear to underpredict turbulence quantities to some extent, especially in the flow discharge region. However, RSM, owning to its superior Reynolds stress modeling, predicts the Reynolds stress, *k* and ε fields better than the *k*-ε RNG model.

Conclusions

Particle Image Velocimetry (PIV) measures instantaneous velocities spatially resolved at multiple points simultaneously. Clearly, the design and scale-up of stirred vessel stand to benefit from this state-of-the-art tool. This paper addresses issues such as how to analyze PIV data, validate CFD predictions, and facilitate model improvement.

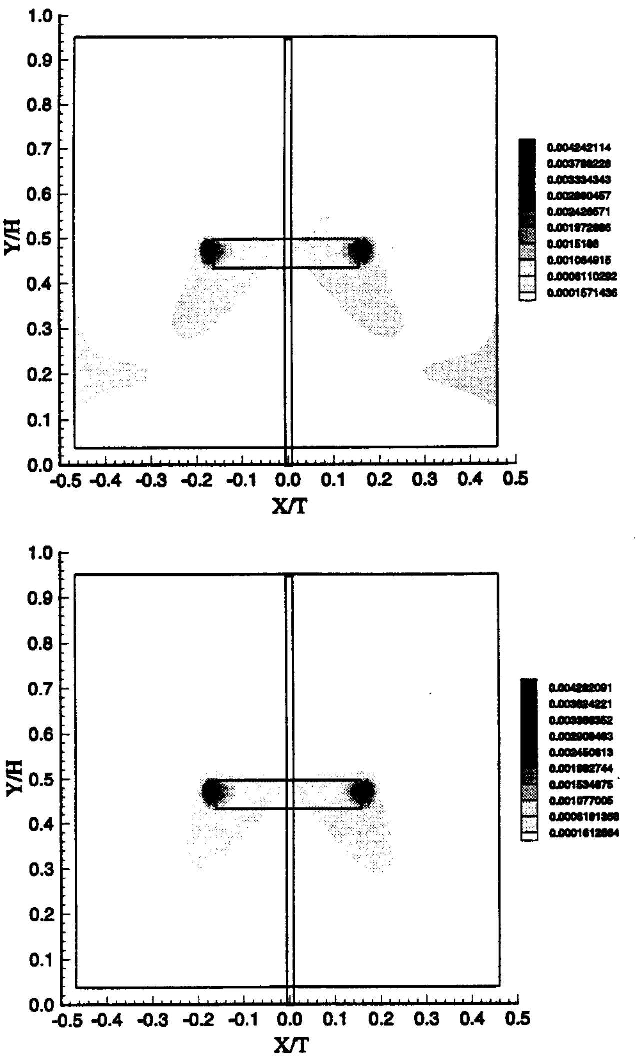

Figure 16 — Reynolds normal stresses predicted by RSM model using LDV boundary conditions . Top: $\langle u'^2 \rangle$. Bottom: $\langle v'^2 \rangle$.

A set of PIV analysis methods are presented to extract time-averaged flow and turbulence fields in a 2D plane in order to compare with RANS simulations. To approximate point-wise time-averaged quantities from spatially filtered PIV data, the Interrogation Cell must be much smaller than the turbulence integral length scale. If the measurement is resolved down to Kolmogorov length scale, the turbulence dissipation rate, ε, can be computed directly by finite-difference approximations from instantaneous PIV data. If PIV resolution lies in the inertial subrange, ε can be approximated from the subgrid scale flux, ε_{SGS}.

In CFD validation studies, the spatial fields processed from PIV data are compared with CFD. Besides visual comparison, several tools are introduced to quantify the similarity and discrepancy between two spatial fields. These tools, including spatial spectrum, correlation and local correlation, prove to be effective. They are applied to the validation of CFD simulations of an axial-impeller stirred vessel.

Various time-independent RANS simulations are conducted using the *k*-ε RNG model and Reynolds Stress Model by Fluent™ with two different boundary conditions and validated against PIV data. Results show that boundary condition setting plays the most consequential role in the prediction of mean flow field. Thus, accurate boundary conditions obtained from experimental data bearing both geometric and dynamic similarity with the simulated flow are required. This may also suggest that the simple scale-up rules (e.g. scaling by tip velocity) widely used for stirred vessel CFD may be insufficient for predicting the correct mean velocity fields.

Results also show that the *k*-ε RNG model, with correctly prescribed boundary conditions at the impeller, predicts the mean velocity pattern rather well without sliding mesh and/or time-dependent CFD. However, relatively large uncertainties in the mean velocity field are found in the high shear regions, the trailing vortex sweeping region and the low Reynolds number swirling flow region near the top of the vessel. Regarding the turbulent fields, the *k*-ε RNG model can qualitatively predict the distribution of kinetic energy, turbulence dissipation rate, and normal Reynolds stresses. In the impeller region, predictions are relatively satisfactory, while in the flow discharge region, CFD simulations underpredict *k*, ε, and normal Reynolds stresses. Examining instantaneous PIV measurements we find a large number of time-varying eddies with various sizes. They account for the underpredictions in the impeller region where the local isotropic assumption used in *k*-ε model are not valid.

Comparing CFD simulations that use different models, no appreciable differences are observed between mean velocity field predictions by the *k*-ε RNG model and RSM. However, greater differences in *k*, ε, and Reynolds stresses are found in simulation results. Reynolds shear stresses cannot be given by *k*-ε RNG model, but they can be qualitatively predicted by RSM, albeit at much smaller values than the experimental results. Both *k*-ε RNG model and RSM generally underpredict *k* and ε , especially in the flow discharge region. We have also demonstrated that accurate boundary conditions obtained from experimental models bearing both geometric and dynamic similarity with the simulated flow are required to correctly predict the mean flow.

The current PIV measurements are limited to two components resolved in a 2D plane. The lack of tangential velocity results in missing terms in *k*, ε, and Reynolds stresses. In general, the effect of these missing terms cannot be easily evaluated due to the anisotropicity of the flow. Furthermore for a 3D flow, PIV data resolved on 2D planes provide, at most, validation of a subset of the 3D flow. Clearly, fully resolved 3-component velocity measurement in a 3D volume as a function of time would be desirable. We expect that further developments of PIV technique into 3D measurement (stereoscopic PIV, Particle Tracking Velocimetry, and Holographic PIV) will pave the way to addressing this need.

Acknowledgement

The authors thank A. Bakker of Chemineer, Inc. and K. J. Myers and R. W. Ward of University of Dayton for providing the PIV data in the stirred vessel used in this study. We thank C. K. Lee from Dow Chemical Company to for his LDV data. Support from NSF grants CTS-9625307 (HM) and CTS-9158124 (ROF), a matching grant from the Dow Chemical Company for the development and application of holographic PIV, and a Special Group Research Incentive Award from KSU are greatly appreciated. We also acknowledge R. S. Brodkey for many helpful discussions.

Nomenclature

A = local comparison area, m^2
C = impeller off-bottom clearance, dimensionless
D = impeller diameter, m

f_x, f_y = wave number along x and y direction, m^{-1}
k = turbulent kinetic energy, m^2/s^2 = J/kg
L = integral length scale, m
N_{Re} = Reynolds number, dimensionless
R_{11} = auto-correlation function of field S_1
R_{12} = cross correlation function of fields S_1 and S_2
R_{22} = auto-correlation function of field S_2
$S(x, y)$ = two-dimension field
$\tilde{S}(f_x, f_y)$ = spectrum of field $S(x,y)$
S'_{ij} = fluctuation strain rate tensor, s^{-1}
$\bar{S}_{ij}$ = resolved strain rate tensor, s^{-1}
T = tank diameter, m
u = radial velocity component, m/s
u' = fluctuation radial velocity component, m/s
u_i = true point-wise instantaneous velocity, m/s
$\bar{U}_i$ = resolved instantaneous PIV velocity, m/s (same as u, v, w)
$\langle \bar{U}_i \rangle$ = time-averaged PIV velocity, m/s (same as u, v, w)
$U(x)$ = mean radial velocity component, m/s
$\langle u' u' \rangle$ = radial normal stress, m^2/s^2
$\langle u' v' \rangle$ = Reynolds shear stress, m^2/s^2
v = axial velocity component, m/s
v' = fluctuation axial velocity component, m/s
$V(x)$ = mean axial velocity component, m/s
V_{12} = local correlation of fields S_1 and S_2, dimensionless
$\langle v' v' \rangle$ = axial normal stress, m^2/s^2
w = circumferential velocity component, m/s
w' = fluctuation circumferential velocity component, m/s
W = turbine blade width, m
x_0, y_0 = origin of comparison area for local correlation calculation, m

Greek letters

δ = comparison length scale for local correlation calculation, m
Δ = filter width, m
ε = turbulence dissipation rate, m^2/s^3 = W/kg
ε_{SGS} = subgrid scale (SGS) dissipation rate, m^2/s^3 = W/kg
η = Kolmogorov length scale, m
ν = kinematic viscosity, m^2/s
τ_1, τ_2 = linear shifts of correlation function along x and y, m
$\bar{\tau}_{ij}$ = SGS stresses, m^2/s^2

References

Adrian, R. J., S. M. Soloff, Z. Liu, C. D. Meinhart and W. Lai, "Stereoscopic PIV Applications to the Study of Turbulence", Proceedings of The Second International Workshop on PIV'97, Fukui, Japan, 75–84 (1997).

Bakker, A., K. J. Myers, R. W. Ward and C. K. Lee, "The Laminar and Turbulence Flow Pattern of a Pitched Blade Turbine", Trans. I. Chem. E. **74**, 485–491 (1996).

Bakker, A. and H. E. A. van den Akker, "Single-phase flow in stirred reactors", Trans. I. Chem. E. **72**, 583–593 (1994).

Calabrese, R. V. and C. M. Stoots, "Flow in the Impeller Region of a Stirred Tank", Chem. Eng. Prog. **85**, 43–50 (1989).

Fluent Inc., "Fluent User's Guide", Version 4.3, Chapter 19, 2–40 (1995).

Fokema, M. D., S. M. Kresta and P. E. Wood, "Importance of Using the Correct Impeller Boundary Conditions for CFD Simulations of Stirred Tanks. Can. J. Chem. Eng. **72**, 177–183 (1994).

Guezennec, Y. G., R. S. Brodkey and J. C. Kent, "Algorithms for Fully Automated Three-Dimensional Particle Tracking Velocimetry", Exp. Fluids **17**, 209–213 (1994).

Jaworski, Z. and I. Fort, "Energy Dissipation Rate in a Baffled Vessel with Pitched Blade Turbine Impeller", Colln Czech Chem Commum. **56**, 1856–1867 (1991).

Kresta, S. M. and P. E. Wood, "Prediction of Three-Dimensional Turbulence Flow in Stirred Tanks", AIChE J. **37**, 448–460 (1991).

Kresta, S. M. and P. E. Wood, "The Flow Field Produced by a Pitched Blade Turbine: Characterization of the Turbulence and Estimation of the Dissipation Rate", Chem. Eng. Sci. **48**, 1761–1773 (1993).

Meng, H. and F. Hussain, "In-line Recording and Off-Axis Viewing Technique for Holographic Particle Velocimetry", Appl. Opt. **34**, 1827–1840 (1995).

Ranada, V. V. and J. B. Joshi, "Flow Generated by Pitched Blade Turbines II: Simulation Using k-ε Model", Chem. Eng. Comm. **81**, 225–248 (1990).

Rao, M. A. and R. S. Brodkey, "Continuous FLow Stirred Tank Turbulence Parameters in the Impeller Stream", Chem. Eng. Sci. **27**, 137–156 (1972).

Sheng, J., H. Meng, and R. O. Fox, "A Large Eddy PIV Method for Turbulence Dissipation Rate Estimation", Chem. Eng. Sci., under revision, (1998).

Smagorisky, J, "General Circulation Experiments with the Primitive Equation I the Basic Experiment", Monthly Weather Review **91**, 99–164 (1963).

Stoots, C. M. and R. V. Calabrese, "Mean Velocity Field Relative to a Rushton Turbine Blade.", AIChE J. **41**, 1–11 (1995).

Van't Riet, K., W. Bruijin and J. M. Smith, "Real and Pseudo-Turbulence in the Discharge Stream from a Rushton Turbine", Chem. Eng. Sci. **31**, 407–412 (1975).

Van't Riet, K. and J. M. Smith, "The Trailing Vortex System Produced by Rushton Turbine Agitators", Chem. Eng. Sci. **30**, 1093–1105 (1975).

Ward, R. W., "A DPIV Investigation of Flow Pattern Instabilities of Axial-Flow Impellers", M.S. thesis, University of Dayton, Dayton, OH, (1995).

Wu, H., G. K. Patterson and M. Van Doorn, "Distribution of Turbulence Energy Dissipation Rates in a Rushton Turbine Stirred Mixer", Exps. in Fluids **8**, 153–160 (1989).

Wu, H. and G. K. Patterson, "Laser Doppler Measurements of Turbulent Flow Parameters in a Stirred Mixer", Chem. Eng. Sci. **44**, 2207–2221 (1989).

Xu, Y. and G. McGrath, "CFD Predictions of Stirred Tank Flows", Chem. Eng. Res. Des. **74**, 471–475 (1996).

Yianneskis, M., Z. Popiolek and J. H. Whitelaw, "An Experimental Study of the Steady and Unsteady Flow Characteristics of Stirred Reactors", J. Fluid Mech. **175**, 537–555 (1989).

Manuscript received October 29, 1997; revised manuscript received April 1, 1998; accepted for publication June 3, 1998.